Transp Porous Med (2005) 58:63–86
DOI 10.1007/s11242-004-5470-8

Pore-Network Modeling of Isothermal Drying in Porous Media

A. G. YIOTIS[1,2], A. K. STUBOS[1,*], A. G. BOUDOUVIS[2], I. N. TSIMPANOGIANNIS[3] and Y. C. YORTSOS[4]

[1]*National Center for Scientific Research "Demokritos"-IPTA, Ag. Paraskevi Attikis, 15310 Athens, Greece*

[2]*School of Chemical Engineering, National Technical University of Athens, 15780 Athens, Greece*

[3]*Los Alamos National Laboratory, Earth & Environmental Sciences Division (EES-6), Los Alamos, NM 87545, USA*

[4]*Department of Chemical Engineering, University of Southern California, Los Angeles, CA 90089-1211, USA*

(Received: 24 July 2003; in final form 22 April 2004)

Abstract. In this paper we present numerical results obtained with a pore-network model for the drying of porous media that accounts for various processes at the pore scale. These include mass transfer by advection and diffusion in the gas phase, viscous flow in the liquid and gas phases and capillary effects at the liquid–gas interface. We extend our work by studying the effect of capillarity-induced flow in macroscopic liquid films that form at the pore walls as the liquid–gas interface recedes. A mathematical model that accounts for the effect of films on the drying rates and phase distribution patterns is presented. It is shown that film flow is a major transport mechanism in the drying of porous materials, its effect being dominant when capillarity controls the process, which is the case in typical applications.

Key words: drying, films, corner flow, pore network

1. Introduction

Drying of porous media is a subject of significant scientific and applied interest. It is involved in the industrial drying of products such as food, paper, textile, wood, ceramics, granular and building materials, etc. Drying is also involved in distillation and vaporization processes associated with soil remediation (Ho and Udell, 1995), as well as in the recovery of volatile oil components from reservoirs by gas injection (Le Gallo *et al.*, 1997).

In general, a single- or multi-component liquid phase gradually evaporates during drying and is removed from the porous structure via combined heat and mass transfer. Traditional descriptions of the process rely

*Author for correspondence: e-mail: stubos@ipta.demokritos.gr

on phenomenological approaches, in which the porous medium is a continuum, the dependent variables, like moisture content, are volume-averaged quantities and the relation of fluxes to gradients is through empirical coefficients. Such approaches essentially ignore the effect of the pore microstructure which is of key importance for a quantitative understanding of the process. Drying is a two phase flow process that involves many pore-scale mechanisms, for example the motion of individual gas–liquid menisci residing in the pore space, diffusion in the gas phase (for a single-component liquid) and the liquid phase (for a multi-component liquid), viscous flow in both phases, capillarity and liquid flow through connected films. All these mechanisms need to be accounted for at the pore scale.

Pore-network approaches are used extensively in recent years to model various processes in porous materials such as drying, immiscible two- and three-phase flow, solution gas-drive and many other (Li and Yortsos, 1995a; Valavanides and Payatakes, 2001; van Dijke *et al*., 2001). Pore network models describe processes at the pore- and pore-network scale and they offer better understanding of the physics involved in these processes than macroscopic continuum models that were used in the past.

Several studies used a pore-network approach to model drying in porous media in recent years. Key to these approaches is the consideration of mass transfer, elements of which were described by Li and Yortsos (1995b) and Jia *et al*. (1999), among others. Various pore-network models with specific applications to drying were proposed originally by Nowicki *et al*., and more recently in a series of papers by Prat and co-workers. Nowicki *et al*. (1992) presented a numerical simulation of the process at the pore-network level without expanding further on the particular patterns and regimes obtained or on the associated effects on drying rates. Prat's studies represent the first attempt to characterize theoretically drying patterns and their rate of change in porous structures. Prat (1995) studied drying patterns assuming capillary control, neglecting viscous effects and considering mass transfer only by quasi-static diffusion. Laurindo and Prat (1996, 1998) also provided a macroscopic assessment of the importance of liquid films that form at the pore walls as the liquid–gas interface recedes. Based on percolation patterns (Wilkinson and Willemsen, 1983) and isothermal conditions, they computed drying rates by solving a quasi-static diffusion equation in the gas phase. Prat and Bouleux (1999) focused on diffusional mass transfer and the effect of gravity on the front structure, but also commented on viscous effects.

In earlier experiments using horizontal glass-bead packs (Shaw, 1987), viscous forces were found to be important for explaining the formation of an evaporating front (separating continuous liquid from gas) of a finite size. More generally, we expect that advection and viscous effects will have an impact on patterns and drying rates. Existing pore-network models

address mostly slow drying, controlled by capillarity and/or gravity and by diffusion, ignoring advection and/or viscous effects. They also neglect the role of liquid films in the process.

In the first part of this paper we present numerical results from a pore network simulator for the drying of porous media that accounts for all major mechanisms at the pore scale but ignores the effect of liquid films. We study mechanisms that have not been accounted for before such as viscous flow in both the gas and the liquid phases and the effect of viscous flow on the movement of the liquid–gas interface. A detailed description of this first part, including mathematical formulation, the algorithm and more extensive results can be found in a recent publication of the present authors (Yiotis *et al*., 2001). In the second part of the paper, the presence of liquid films is considered. We model capillarity-driven liquid flow in a 2D pore network and propose a mathematical model that accounts for viscous flow in the liquid films as well as all the other mechanisms presented earlier. This part is a detailed description of the study by Yiotis *et al*. (2003) (published elsewhere as a brief report) and an extension of that work.

2. Pore-Network Modeling of Drying without the Presence of Liquid Films

We consider the isothermal drying of a fractured porous medium initially saturated with a volatile liquid. The liquid is trapped in the pore space due to capillary forces and may vaporize as a result of an injected purge gas flowing primarily in the fractures. This process is applied to enhance oil recovery from reservoirs (Stubos and Poulou, 1999).

The actual overall problem is quite complex, requiring the consideration of the network of fractures and the medium continuum, gas flow and mass transfer in the fracture network and the multi-dimensional mass transfer from the medium continuum to the fracture network. For simplicity, we consider a 2D square pore network with all but one boundaries impermeable to flow and mass transfer (Figure 1).

At any time during the process, evaporation of the liquid at the liquid–gas interface leads to the receding of the liquid front (denoted as evaporating interface (I) or percolation front (P) in Figure 1), leaving behind disconnected clusters of liquid and liquid films, the size and location of which change continuously with time. In general, three different spatial regions can be identified:

(i) a far-field (from the fracture) region consisting of the initial liquid (continuous liquid cluster, CC);
(ii) a region where the liquid phase is disconnected and consists of individual liquid clusters of variable sizes (disconnected clusters, DC); and
(iii) a near-field (to the fracture) region consisting primarily of the continuous gas phase, with the liquid phase in the form of pendular rings,

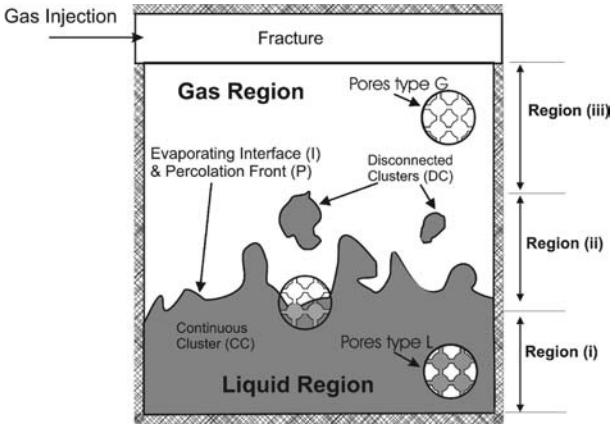

Figure 1. Schematic representation of a drying process in a 2D matrix driven by the injection of a purge gas through a fracture along the upper size of the matrix.

corner films or thin films on the solid surface, the thickness of which is progressively reduced towards a "totally dry" regime.

In Figure 1, the fracture running along the upper side of the 2D network is represented as a 1D chain of pore bodies and throats. The two ends of the fracture are open to flow and mass transfer. The network consists of spherical pore bodies connected through cylindrical pore throats. Pore bodies serve as containers for either of the two phases and it is assumed that they have no capillary or flow resistance. Therefore, when a liquid–gas interface lies within a pore body, the pressures of both phases are taken to be equal and the interface recedes without any capillary forces restraining its movement. The throats serve as conductors of the flow and mass transfer and they act as capillary barriers.

Initially the network is saturated by a single-component liquid (hexane). The fracture, however, contains only air at the beginning of the drying process. A purge gas (air) is injected at a constant volumetric rate from one end of the fracture. The concentration of the liquid component vapors is assumed to be zero at the entrance and the exit of the fracture at all times. The gas injection results to a pressure gradient along the fracture, which eventually develops inside the pore network as well. As a result of the gas flow, the liquid evaporates initially at the interface pore throats along the fracture. Vapor flows by advection and diffusion to the exit of the fracture.

Mass transfer of the vapor in the gas phase obeys the convection-diffusion equation

$$\frac{\partial C}{\partial t} + \mathbf{u} \cdot \nabla C = D \nabla^2 C \tag{1}$$

where C is the vapor concentration, D is the diffusion coefficient and $\mathbf{u}$ is the gas-phase velocity vector.

Both in the liquid and gas phases the fluxes Q between adjacent pores are computed by Poiseuille-law type flow resistances, where the viscosity μ is taken constant

$$Q_{i_j} = \left(\frac{P_i - P_j}{\ell} \right) \frac{\pi r_{ij}^4}{8\mu} \tag{2}$$

$$\sum_j Q_{ij} = 0 \tag{3}$$

where P is the pressure at the center of each pore, r_{ij} is the throat radius between pores i and j and ℓ is the distance between pore centers.

Liquid menisci that reside at interface throats recede due to evaporation of the liquid and the gas invades the adjacent liquid pores. We assume that the menisci recede instantly because throats have no volume. At every liquid cluster, at least one liquid pore empties at any time during drying while all other liquid menisci may remain stationary due to capillary forces. A pore is invaded when the pressure difference across its throats exceeds the capillary pressure threshold $2\gamma/r$, where γ is the surface tension. If the pressure difference is not sufficiently large and all menisci of a cluster are pinned then the pore where the pressure difference is closer to its throats' capillary pressure threshold is invaded.

The problem is mainly characterized by two dimensionless parameters, a diffusion-based capillary number, Ca_D, and a Peclet number, Pe, in addition to the various geometrical parameters of the pore network

$$Ca_D = \frac{D\mu_{\mathrm{l}} C_{\mathrm{e}}}{\gamma \ell \rho_{\mathrm{l}}} \tag{4}$$

$$Pe = \frac{V_{\mathrm{f}} \ell}{d} \tag{5}$$

where C_{e} is the equilibrium concentration of the vapor, V_{f} is the mean velocity of the purge gas in the fracture and the liquid phase is denoted by subscript l. The capillary number expresses the ratio of viscous to capillary forces, based on a diffusion-driven velocity, while the Peclet number expresses the ratio of inertial to diffusion forces. We note that liquid films are neglected in this formulation. The details of the algorithm followed for the numerical solution of the problem can be found in Yiotis *et al.* (2001).

We present here two runs on a 50×50 pore network that are characteristic of the two limiting regimes that develop in this process. In the first run the gas flow rate through the fracture is very low and the process is characterized by a very low value for the Peclet number ($Pe = 0.66$ – run 15) (Figures 2 and 4). In this case capillary forces are dominant and mass

transfer occurs primarily by diffusion. In the second run the purge gas is injected at a very high flow rate leading to a very high value of the Peclet number ($Pe = 331$ – run 4) (Figures 3 and 5). In this case viscous forces dominate at the liquid–gas interface while mass transfer occurs primarily by advection.

In the low Peclet number case, viscous forces are not sufficiently strong and the capillary pressure variation is negligible at the perimeter of liquid clusters. Assuming the absence of liquid films that could provide hydraulic conductivity between macroscopically disconnected liquid clusters (DCs) and the continuous liquid cluster (CC), every cluster takes the pattern of

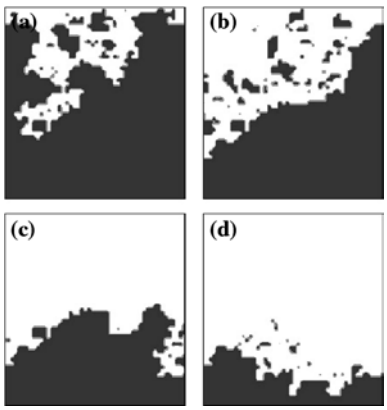

Figure 2. Phase distribution patterns for a low Peclet number ($Pe = 0.66$ – run 15). The process follows Invasion Percolation rules at all times. Air is white and liquid hexane is black.

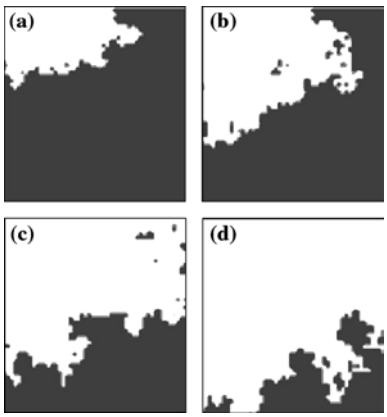

Figure 3. Phase distribution patterns for a high Peclet number ($Pe = 331$ – run 4). At early stages the process follows Invasion Percolation in a Stabilizing Gradient rules. Later on patterns become Invasion Percolation-like. Air is white and liquid hexane is black.

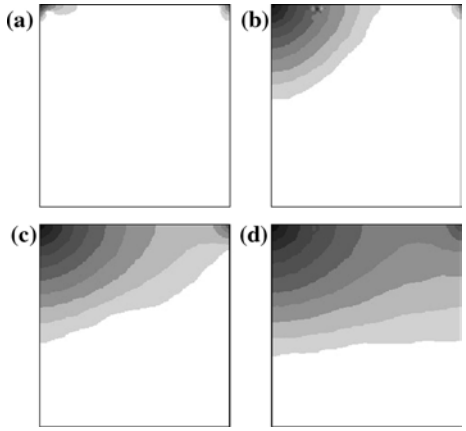

Figure 4. Concentration contours for a low Peclet number case ($Pe = 0.66$ – run 15). The snapshots correspond to the phase distribution patterns shown in Figure 2. Darker colors indicate lower vapor concentration.

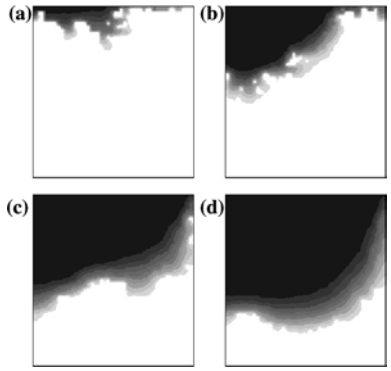

Figure 5. Concentration contours for the high Peclet number case ($Pe = 331$ – run 4). The snapshots correspond to the phase distribution patterns shown in Figure 3. Darker colors indicate lower vapor concentration.

Invasion Percolation (IP), in which the next throat to be invaded by the gas is that with the smallest capillary threshold (here, the one with the largest size) among all perimeter throats of that cluster (Figure 2). In the related study of Li and Yortsos (1995a, b) this process was termed *local percolation*.

Clusters closer to the open boundary are subject to a faster evaporation, compared to those further away, and are emptied faster (Figure 4). The end result is the development of gradients in the size of the isolated liquid clusters, with clusters closer to the fracture having smaller size. These gradients reflect mass transfer, rather than viscous effects. Clearly, however, the overall pattern would be a function of the drying rates, namely of the value of

the *Pe*. We must note that under this regime of local percolation, different clusters may have different-size throats being invaded at the same time.

In the high Peclet number case the process is controlled by viscous forces and capillarity is negligible at early times (Figure 3). Pore throats closer to the inlet of the fracture, where the gas is injected, are subject to stronger viscous effects than pore throats away form the fracture. Phase distribution patterns deviate substantially from IP and almost follow a piston-like displacement (PD). The receding of the CC has some of the properties of IPSG in a fracture-matrix system. Under these conditions, the capillary resistance of a throat is negligible, and the pattern is exclusively determined by mass transfer considerations, much like in the dissolution of a solid. The rate of generation of DCs and their size are smaller and the liquid phase consists mostly of a CC. As the liquid–gas interface recedes in the pore network away from the fracture, viscous forces become weaker and the process gradually becomes of IP type, namely controlled by capillarity.

Concentration contours for these two limiting cases are shown in Figure 4 for the low Peclet number case and Figure 5 for the high Peclet number case. The concentration contours are smoother in the first case because mass transfer is controlled by diffusion. In the second case, the concentration contours are very steep close the liquid–gas interface and the vapor concentration is very low close to the fracture.

Typical drying curves for the process are presented in Figure 6. The high Peclet number case ($Pe = 331$) shows a clear constant rate period (CRP) for the drying rate that lasts approximately as long the CC remains in contact with the fracture. This CRP is much shorter for lower values of the Peclet number (i.e. $Pe = 132$) because the CC recedes form the fracture sooner (with respect to the liquid recovery volume). However, the overall drying rate is much shorter in the high Peclet number case as expected. More results and discussion including cases of intermediate Peclet numbers are shown in Yiotis *et al.* (2001).

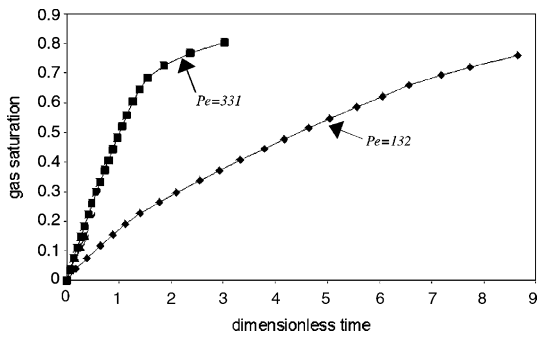

Figure 6. Drying curves for various Peclet numbers.

3. The Effect of Liquid Films

In this section we study the role of wetting films in the context of drying. The objective is to determine if film flows can be a significant mechanism of drying as purported to be in the experiments cited below. A 2D pore-network model, very similar to the one described above, is used for the representation of the porous medium. In this case however we consider that the velocity of the purge gas in the fracture is very low and that viscous forces due to flow in the gas phase on the liquid–gas interface are negligible. Our focus is on the effect of viscous flow through the liquid films that develop at the corners of the pore network.

Flow through macroscopic films has been analyzed in the context of imbibition by many authors (Lenormand and Zarcone, 1984; Lenormand, 1992; Dullien *et al*., 1989; Constantinides and Payatakes, 2000). Lenormand (1992) described in detail the expected mechanisms due to film flow in imbibition. Dullien *et al*. (1989) reported flow along surface microchannels that provide hydraulic connectivity between macroscopically isolated liquid regions during immiscible displacement in packed glass beads with rough surfaces. This was found to be negligible in the case of smooth glass beads. Dillard and Blunt (2000) examined mass transfer from liquid films in dissolution processes, while Blunt *et al*. (2002) presented a detailed review of flow through films in the context of three-phase flow.

In the context of drying, past experimental work has emphasized the existence and speculated on the role of film flow (Shaw, 1987; Laurindo and Prat, 1998; Tsimpanogiannis *et al*., 1999). In a series of experiments Shaw (1987) found that, under comparable conditions, the drying front in a cell containing packed beads moved one order of magnitude faster than when the cell was empty. Shaw attributed this "unorthodox" result to liquid counterflow through films which form along particle contacts, and argued that it is the dominant mechanism for the drying of porous materials. Laurindo and Prat (1998) performed drying experiments in two-dimensional etched-glass micromodels and compared their results with predictions from a pore-network simulator, which did not contain films. The experimental rates were found to be about six times higher than the numerical. These authors also attributed the flow enhancement to wetting liquid films and presented a simplified model for the associated transport mechanism. Liquid films were described in the form of a bundle of microcapillaries on the pore surface. However, no quantitative models for film flow were developed in these studies.

3.1. PROBLEM FORMULATION

We consider the isothermal evaporation of a single-component liquid in a porous medium one side of which is open to the environment. The latter

is kept dry through the flow of a purge gas, while all other three sides are impermeable to fluid flow and mass transfer. The porous medium is again represented by a 2D square lattice of pores connected through throats with square cross-section. The radii of the throats, hence the corresponding capillary thresholds, are distributed randomly. In the presence of films, at any stage of drying, the pore space can be characterized by three kinds of pores (close-ups in Figure 7): pores L, fully occupied by liquid, pores G, fully occupied by gas, and pores F, occupied by gas but also containing liquid films. The existence of pores of type F is the distinguishing feature of this work, compared to previous (Prat, 1995; Laurindo and Prat, 1998; Prat and Bouleux, 1999; Tsimpanogiannis *et al.*, 1999; Yiotis *et al.*, 2001, Plourde and Prat, 2003). Our focus is on thick films, e.g. which form in the corners of polygonal pores, and where flow is driven by capillary pressure gradients. Here, we will account for viscous effects both in the films (F pores), as well as in the continuous liquid phase (region L). Mass transfer in the gas phase is assumed only by diffusion, which is usually valid in drying problems (Prat, 1995; Laurindo and Prat, 1996, 1998).

Due to the applied concentration gradients, the liquid evaporates along the liquid–gas interfaces and the liquid vapors are transferred by diffusion in the gas phase towards the dry end. During this process, the macroscopic gas–liquid interfaces (denoted by P in Figure 7) recede, both in the continuous and the discontinuous clusters.

3.2. LIQUID FLOW THROUGH MACROSCOPIC FILMS IN A SINGLE CAPILLARY

We first study the case of long capillary with square cross-section where the liquid meniscus has just receded leaving behind liquid films at the four corners of the capillary (Figure 8). The thickness of each liquid film can

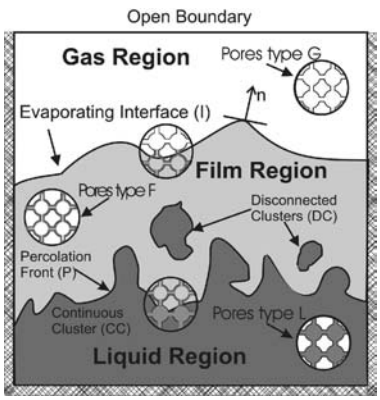

Figure 7. Schematic of liquid and gas phase patterns, indicating the various types of pores in drying used in this study.

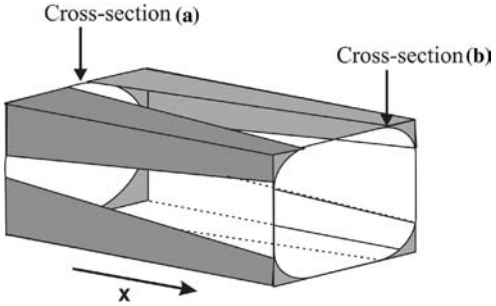

Figure 8. Liquid films along the corners of a capillary with square cross-section.

be parameterized by its radius of curvature r, which is a function of time and distance. We assume that all four films have the same thickness at any cross-section along the capillary. Assuming local capillary equilibrium at the film interface, we have

$$P_c = P_g - P_l = \frac{\gamma}{r} \tag{6}$$

By neglecting variations in the gas pressure, we can take without loss, $P_g = 0$. Then, the pressure in the film, P_l, is

$$P_l = -\frac{\gamma}{r} \tag{7}$$

According to Equation (7) the liquid pressure in the film is inversely proportional to its thickness. Any gradient in the film thickness along the capillary results in a pressure gradient along the liquid films. A capillarity-induced flow develops along the film from the cross-section where the film is thicker (Figure 9(a)) towards the cross-section where the film is thinner (Figure 9(b)).

Several authors (Lenormand and Zarcone, 1984; Ransohoff and Radke, 1988; Zhou *et al.*, 1997) have studied film flow along the corners of long smooth capillaries with polygonal cross-sections. Assuming uni-directional

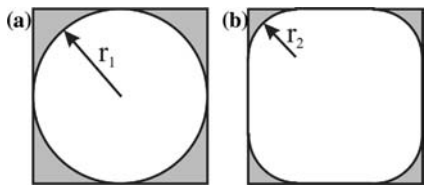

Figure 9. Evolution of the film radius that develops at the corners of a capillary with square cross-section. Cross-section (a) is closer to the bulk liquid phase and the films are thicker than in cross-section (b).

(direction x) viscous flow, a Poiseuille-type law applies in these geometries,

$$Q_x = -\frac{\alpha r^4}{\mu_l}\frac{\partial P_l}{\partial x} \tag{8}$$

where Q_x is the volumetric flow rate and α is a dimensionless geometric factor. By combining Equations (7) and (8), we obtain

$$Q_x = -\frac{\alpha\gamma r^2}{\mu_l}\frac{\partial r}{\partial x} \tag{9}$$

Parameter α was determined previously for various model geometries (Ransohoff and Radke, 1988, Dong and Chatzis, 1995). The latter authors studied film flow in one corner of a capillary with a polygonal cross-section and found the following expression

$$\alpha = \frac{C^*}{\beta} \quad \text{where } C^* = 4\left(\frac{\cos\theta\cos(\pi/4+\theta)}{\sin(\pi/4)} - (\pi/4-\theta)\right) \tag{10}$$

the shape factor C^* being expressed in terms of the contact angle θ. The dimensionless resistance β was earlier calculated by Ransohoff and Radke (1988). In the case of a capillary with square cross-section and a perfect wetting liquid ($\theta = 0$) we have $C^* = 4-\pi$, $\beta = 93.5$ and $\alpha = 0.0088$. We note that parameter α is of order 10^{-3}.

We consider the mass balance for the evaporating liquid in the capillary

$$(4-\pi)\frac{\partial r^2}{\partial t} = -\frac{\partial Q_x}{\partial x} - Q_{ev} \tag{11}$$

where Q_{ev} is the evaporation rate. Assuming a simple diffusion model we take

$$Q_{ev} = \left(\frac{2\pi r D}{\rho_l}\right)\frac{(C_e - C)}{r_0} \tag{12}$$

where C is the average gas-phase mass concentration (mass per unit volume) of the evaporating liquid and r_0 is the radius of curvature where the films emanate. The particular details of film evaporation, particularly near the tip of the film are very complex. Equation (12) is only a first-order approximation, and the value of D acts as a lumped parameter to account for many of the neglected phenomena.

Combining Equations (9), (11) and (12) leads to

$$\frac{\partial r}{\partial t} = \frac{2\alpha\gamma}{(4-\pi)\mu_l}\left[r\frac{\partial^2 r}{\partial x^2} + 2\left(\frac{\partial r}{\partial x}\right)^2\right] - \frac{\pi D}{(4-\pi)\rho_l}\frac{(C_e - C)}{r_0} \tag{13}$$

For dimensionless notation, we introduce the diffusive time $\tau = \frac{Dt}{r_0^2}$, a rescaled radius of curvature, $\rho = \frac{r}{r_0}$, a rescaled axial distance, $\xi = \frac{x}{r_0}$, and a dimensionless concentration $\zeta = \frac{C}{C_e}$ based on which we write

$$\left(\frac{(4-\pi)\rho_l}{\pi C_e}\right) Ca_F \frac{\partial \rho}{\partial \tau} = \rho \frac{\partial^2 \rho}{\partial \xi^2} + 2\left(\frac{\partial \rho}{\partial \xi}\right)^2 + Ca_F(\zeta - 1) \tag{14}$$

Here we introduced the capillary number in the form $Ca_F = \frac{\pi D C_e 2\mu_l \beta}{\rho_l C^* r_0 \gamma}$. As in other mass-transfer driven processes, this capillary number expresses the ratio of the viscous forces due to flow driven by mass transfer to capillary forces.

The mass balance in the gas phase reads

$$\frac{\partial C}{\partial t} = D\frac{\partial^2 C}{\partial x^2} + \frac{1}{2}\frac{\pi r D}{r_0^3}(C_e - C) \tag{15}$$

and in dimensionless notation,

$$\frac{\partial \zeta}{\partial \tau} = \frac{\partial^2 \zeta}{\partial \xi^2} + \frac{1}{2}\pi\rho(1-\zeta) \tag{16}$$

Equations (14) and (16) are coupled and solved for the dimensionless film thickness ρ and the dimensionless concentration ζ as a function of time τ and capillary length ξ with the appropriate initial and boundary conditions. We find that for realistic values of the capillary number Ca_F, a steady-state profile for ρ and ζ is quickly established (Figure 10). This is consistent with other diffusion-controlled problems in porous media (Witten and Sanders, 1981; Peitgen and Saupe, 1988). In addition, the restriction of the evaporation to a narrow region is a consequence of the exponential decay of the concentration: Due to the confined pore geometry, the gas phase becomes rapidly saturated, limiting evaporation to a narrow region near the film tips, where the liquid flux is supplied by capillarity-driven film flow (Yiotis *et al.*, 2003).

Given that $\zeta = 1$ along the film region and that a steady-state profile for ρ is quickly established, Equation (14) can be simplified as follows

$$\rho\frac{\partial^2 \rho}{\partial \xi^2} + 2\left(\frac{\partial \rho}{\partial \xi}\right)^2 = 0 \Rightarrow \frac{\partial^2 \rho^3}{\partial \xi^2} = 0 \tag{17}$$

In the dry region, between the film tip and the open end of the capillary, the film thickness is $\rho = 0$ and liquid vapors are transferred by diffusion towards the open end of the capillary. Equation (16) becomes

$$\frac{\partial^2 \zeta}{\partial \xi^2} = 0 \tag{18}$$

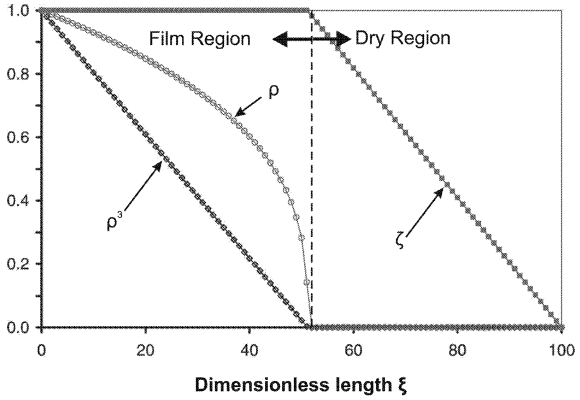

Figure 10. Steady-state profiles for the dimensionless film thickness ρ and vapor concentration ζ along a single capillary. The film emanates at $\xi = 0$.

We note that Equations (17) and (18) apply along the film and in the totally dry part of the capillary, respectively. The mass balance at the film tip reads

$$\frac{\pi}{6Ca_F}\frac{\partial \rho^3}{\partial \xi} = \frac{\partial \zeta}{\partial \xi} \quad \text{and } \rho = 0, \ \ \zeta = 1 \tag{19}$$

Given that the location of film tip is unknown, we consider a simple transformation that leads to a rather straightforward solution.

$$\Phi \equiv \frac{\rho^3 + \zeta Ca_F}{1 + Ca_F} \tag{20}$$

Function Φ satisfies Equations (17) and (18) in their domains and is continuous at the film tip. Equations (17) and (18) can be replaced by

$$\frac{\partial^2 \Phi}{\partial \xi^2} = 0 \tag{21}$$

The location of the film tip is calculated from the solution of Equation (21) by applying the appropriate boundary conditions at the beginning of the film and the open end of the capillary. Note that in our model the distance of the film tip from the open end of the capillary actually determines the effect of films in the drying process. The closer is the film tip to the open end of the capillary the higher is the drying rate.

3.3. DRYING THROUGH MACROSCOPIC FILMS IN A PORE NETWORK

The single-capillary physics described above are also expected to apply to the general problem, where films exist in a network of pores connected

through capillaries similar to the one considered above. As described in Section 3.1, the gas region of such a network contains F pores adjacent to capillaries that contain films (film region) and G pores adjacent to dry capillaries (dry region) (Figure 7). Given that Equation (17) applies in the film region of a single capillary, we can assume that the film thickness in the film region of a 2D pore network is described by the following Laplace equation

$$\nabla^2 \rho^3 = 0 \tag{22}$$

Assuming a quasi-steady state in the concentration in dry region and evaporation occurring where the films terminate, namely at the interface I between pores F and G, the vapor concentration in the dry region is described by the following Laplace equation

$$\nabla^2 \zeta = 0 \tag{23}$$

The mass balance at the film tips where the liquid evaporates (interface I in Figure 7) reads

$$\frac{\pi}{6Ca_F}\frac{\partial \rho^3}{\partial n} = \frac{\partial \zeta}{\partial n} \quad \text{and } \rho = 0, \ \ \zeta = 1 \tag{24}$$

The film region is saturated with liquid vapors, $\zeta = 1$, and the film thickness is zero in the dry region, $\rho = 1$.

Assuming that we know the location of the percolation front P at any time, we can solve the full problem using the transformation proposed in Section 3.2. Equations (22) and (23) become

$$\nabla^2 \Phi = 0 \text{(in regions G and F)} \tag{25}$$

We assume that the film thickness ρ is approximately constant at the percolation front P

$$\Phi = 1 \text{ at the percolation front P} \tag{26}$$

and that drying is driven by imposing $\zeta = 0$ at the open side of the network

$$\Phi = 0 \text{ at the open end of the network} \tag{27}$$

Using the above transformation, the solution of the Laplace equation (25) can be used to determine the profiles of the film radius and the concentration, the rates of drying through each film, as well as the location of the interface I, where the films terminate and evaporation occurs. Interface I is located simply as the position where

$$\Phi = \frac{Ca_F}{Ca_F + 1} \tag{28}$$

The location of the percolation front P is determined by solving for the liquid fluxes in the liquid phase and films, simultaneously. In all pores occupied fully by liquid (pores of type L), the viscous flow is described by Poiseuille-type expressions. For these pores, the liquid mass balance at any pore i reads in dimensionless notation

$$\sum_j (p_i - p_j)\sigma_{ij}^4 = 0 \tag{29}$$

where j denotes a neighboring pore, σ is the normalized pore radius, and we have normalized pressure drops with the characteristic value $P^* = \frac{\gamma}{r_0}$. For pores at the perimeter P, however, the mass balance is different and we need to further distinguish two cases.

If the pressure difference at a pore that belongs to the percolation front is not sufficiently large for the gas phase in the neighboring pore to penetrate the connecting throat, the meniscus remains stationary. Because of the films, however, there is always net liquid outflow from the liquid pore. The mass balance at every such pore at the percolation front reads

$$\sum_j (p_P - p_j)\sigma_{ij}^4 = -\frac{32\alpha}{3\pi}(1 + Ca_F)\sum_F \left.\frac{\partial \Phi}{\partial \xi}\right|_P \tag{30}$$

where the first sum denotes the liquid arriving at the perimeter pore P and the last sum denotes the contributions from the films in pores of type F draining the perimeter pore.

If the capillary pressure at a perimeter throat is sufficiently high, namely if the following condition is satisfied

$$-p_P > \frac{1}{\sigma_{ij}} \tag{31}$$

the adjacent pore is penetrated by the gas phase. As in Yiotis *et al.* (2001), in such pores we assume that the capillary pressure is zero. Then, the corresponding mass balance reads in dimensionless notation

$$\sum_j p_j \sigma_{ij}^4 - \frac{32\alpha}{3\pi}(1 + Ca_F)\sum_F \left.\frac{\partial \Phi}{\partial \xi}\right|_P = \frac{8\mu_1 Q_P}{\pi r_0^2 \gamma} \tag{32}$$

where we have taken $p_P = 0$. Q_P is the flow rate at which the pore empties.

Equations (30) and (32) are solved for the pressure field in the liquid phase and the flow rates Q_P that penetrated pores empty given the solution of the Laplace equation (25) in the gas phase that determines the liquid fluxes through the liquid films at the perimeter of the liquid clusters.

The gas saturation at every pore that has been penetrated by the gas phase is calculated explicitly in time

$$\Delta S_i = \frac{\Delta t}{V_P} \cdot Q_P \tag{33}$$

where V_P is the pore volume, Δt is the time step and Q_P is assumed constant during the time step.

The algorithm used in our simulator is based on the work by Yiotis *et al.* (2001) and can be summurized as follows: At any given time, pores have one of the designations L, F or G (Figure 7). The L pores can be part of the original liquid cluster (CC) or of the disconnected finite-size clusters (DC). At every time step, the overall rate of evaporation from each of the liquid clusters is evaluated using the Laplace equation (25). Pressure fields in the liquid clusters are calculated with Equations (30) and (32) and Partly Empty pores at the percolation front are emptied according to Equation (30). The time step is selected such that it equals the minimum time required to empty completely any of the available Partly Empty pores. If at the current time no Partly Empty pores are available to any (or all) of the clusters (namely if all pores are of the CE type, Yiotis *et al.*, 2001), the throat with the smallest capillary threshold in the perimeter of any given cluster is invaded next, at which time the invaded pore becomes of the PE type. To determine this throat, the liquid pressure is lowered uniformly in space inside the cluster, until the capillary pressure exceeds for the first time the smallest capillary threshold. Invasion must occur, since due to evaporation there is a continuous loss of mass from the liquid clusters through film flow. Then, the interfaces are updated, the equation for Φ is solved again, the rates of flow through the film obtained and the process continues. All calculations are done explicitly in time. The fields for the pressure and Φ are computed using Successive Over-Relaxation.

3.4. NUMERICAL RESULTS AND DISCUSSION

We performed a series of numerical simulations in 100×100 pore networks for different values of Ca_F to study the effect of liquid films on the extent of the liquid films, the phase distribution patterns and drying rates. The pore network consists of spherical pores connected through throats with square cross-section. All pores have the same radius $500\,\mu$m while the size of the throats follows a random distribution between 170 and $270\,\mu$m. We assume that the film flow occurs practically only in the throats that also act as capillary barriers. Pores serve as containers of either of the two phases

3.4.1. *Phase Distribution Patterns*

Equations (30) and (32) show that the pressure drop at the percolation front P (at the perimeter of liquid clusters) scales as $(1 + Ca_F)$. For values of Ca_F less than order of 1 (which is the typical case in most physical problems) we expect that the effect of the capillary number on the phase distribution patterns is negligible. In that range, phase distribution patterns follow Invasion Percolation rules. The left panel in Figure 11 shows two snapshots of the percolation front for $Ca_F = 10^{-4}$ that correspond to IP patterns.

As the capillary number increases, the patterns eventually depart from IP, particularly at the early times of the process. However, Figure 11 shows that quite large capillary number values are needed for a noticeable effect on the pattern. For example, the middle panel of Figure 11 shows that even for $Ca_F = 1$ the pattern is almost identical to IP, except for a few small differences at the start of the process. It takes larger values, of the order of $Ca_F = 10$ (right panel of Figure 11), for the effect to be pronounced. Then, the pressure drop at the front becomes relatively significant, and the pattern exhibits the expected behavior of viscous "stabilization" (Tsimpanogiannis *et al.*, 1999), as Invasion Percolation in a Stabilizing Gradient (IPSG)).

As drying progresses, the recovery rate diminishes due to the receding of the percolation front. In the large Ca_F case, this results to a transition from IPSG patterns to capillary-dominated IP patterns. It follows that under typical conditions and for all practical purposes, the drying front can be accurately described as an IP front. This is in contrast to the behavior of external drainage, where viscous effects on the pattern become important for values of the capillary number as low as 10^{-3}.

3.4.2. *Extent of Liquid Films*

The film properties are determined from the solution of the Laplace equation (25) for Φ. Figure 12 shows a snapshot of the iso-potential contours of Φ around the percolation front of the liquid clusters. The patterns reflect the solution of the Laplace equation around a fractal object, hence following the fractal features at distances close to it, but becoming smooth at a small distance away. Because of the assumed boundary condition $\Phi = 1$ at the cluster perimeter, all clusters act as sinks, therefore there is no fluid flow from one cluster to another.

For low values of Ca_F, which is typically the case, the films extend all the way to the open boundary (where $\Phi = 0$). By contrast, when Ca_F is of order 1, the films are short and the film tips (evaporation interface I) reside closer to the liquid cluster interface P (where $\Phi = 1$).

Figure 13 shows the evolution of the film radius profiles for two values of Ca_F. The film radius has the approximate profile $\rho \propto \xi^{1/3}$ where ξ is the

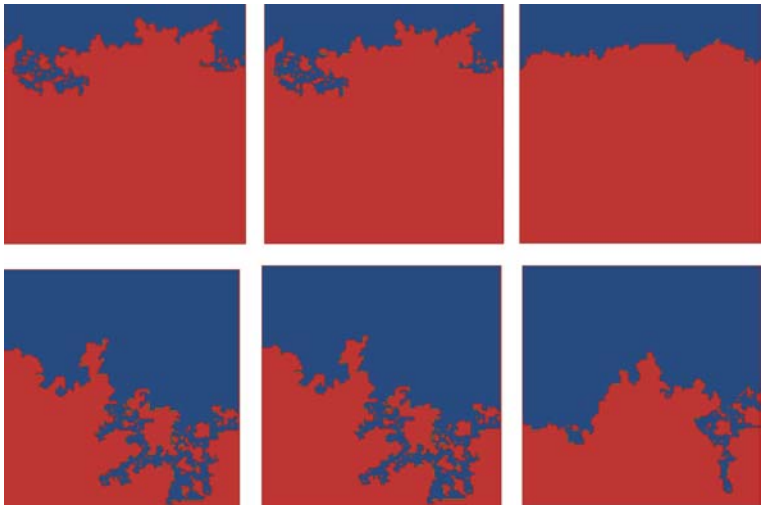

Figure 11. Two snapshots of the drying front for $Ca = 10^{-4}$ (left), $Ca = 1$ (middle) and $Ca = 10$ (right). Liquid-occupied pores are in red.

distance from the front, and which corresponds to the solution of Equation (25), as discussed above. The location of the film tips (interface I) is the contour with the value $\Phi = \frac{Ca_F}{Ca_F+1}$. Figure 13 shows that at low Ca_F (left panel), the films extend all the way to the open end, which is the place where practically all evaporation occurs. When Ca_F is of order 1 or larger, however, the films are shorter (right panel in Figure 13), and lead to the formation of a completely dry region G, the extent of which increases with

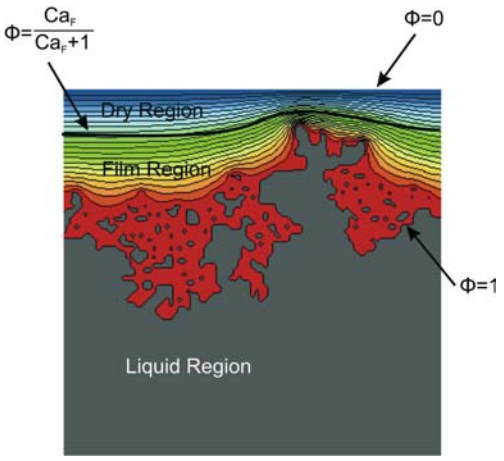

Figure 12. Iso-contours of the solution of the Laplace equation around the liquid clusters, for $Ca = 0.5$, with boundary conditions $\Phi = 1$ at the front and $\Phi = 0$ at the open end.

time. Even though the film region is short and a fully-dry region has developed, the drying front is still of the IP type (as in the left panel). In the O(1) case, the film tips mimic the protuberances of the drying front, being closer to the open boundary if associated with a corresponding protuberance. Films that end at such points will have a larger drying rate, since the gradient of Φ (and of the concentration) there is larger, (Figure 14).

In the typical problem, where the capillary number is generally less than O(1), we anticipate the existence of long films that drain liquid through the above "wicking" action, and all the way to the open end where it subsequently evaporates. For instance, in the experiments in Laurindo and Prat (1996, 1998) we have made the rough estimate $Ca_F \sim 10^{-4}$ suggesting that liquid films (film region F in Figure 7) likely existed in all gas-invaded pores in the experiments and that a completely dry region (gas region G in Figure 7) did not develop, (Figure 13, left panel).

3.4.3. *Drying Curves*

Based on the analysis in Section 3.3 the overall drying rate at the open side of the pore network is

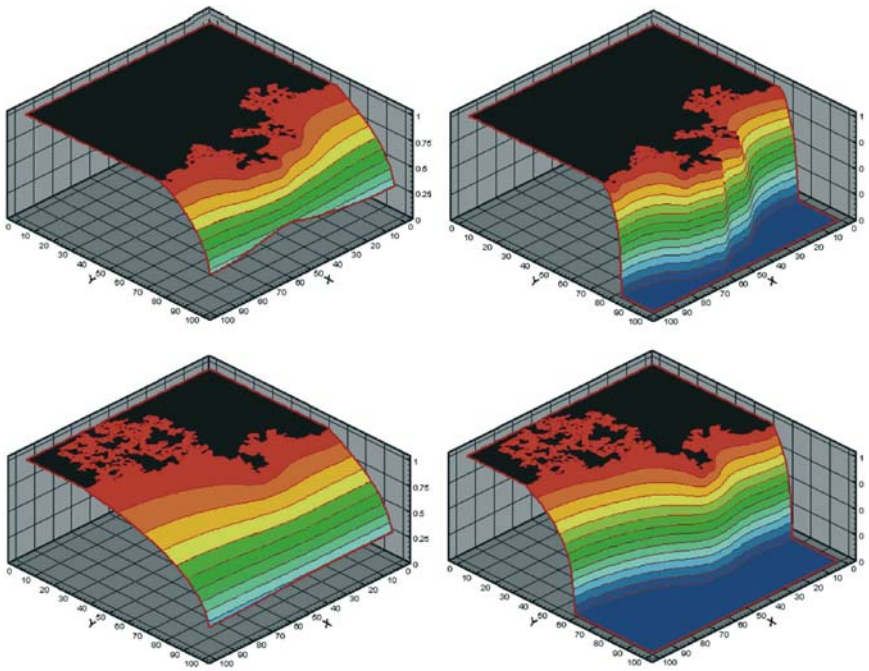

Figure 13. Profiles of the rescaled film radii for $Ca_F = 10^{-4}$ (left) and $Ca_F = 1$ (right) at two different stages of the process. Liquid clusters are in black, the fully dry region is in blue.

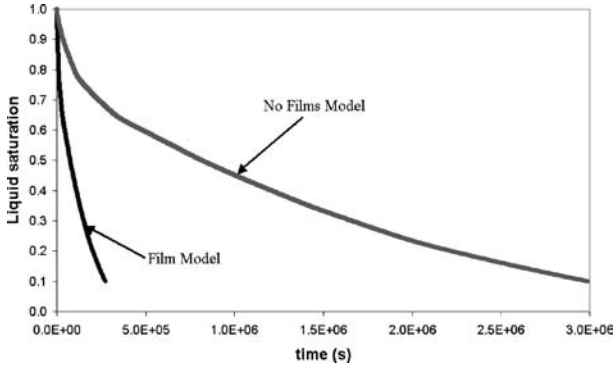

Figure 14. Drying curves calculated with a numerical model that does not account for the effect of liquid films and a model that accounts for liquid films for $Ca_F = 0.1$ under comparable conditions.

$$F = \frac{DC_e r_t^2}{\ell} \frac{1 + Ca_F}{Ca_F} F_D \tag{34}$$

where r_t is the average throat radius along the open boundary, $F_D = -\int_{a_0} \frac{\partial \Phi}{\partial n} da$ is the dimensionless drying rate and subscript 0 denotes the open boundary. The dimensionless rate F_D depends on the geometry of the porous medium.

Equation (34) shows that the drying rate scales as $\frac{Ca_F+1}{Ca_F}$. The drying rate increases as Ca_F decreases and the film tips are closer to the open boundary. At smaller values of Ca_F, capillarity helps to transport liquid over larger distances and to keep the film extent longer. This is favored by larger interfacial tension, larger values of the film thickness r_0 at the percolation front (where films emanate) and smaller viscosity and effective diffusivity. It is readily shown that in the region of small Ca_F, the drying rate scales as

$$F \sim \frac{\gamma r_0}{\mu_1} \tag{35}$$

showing the dominant effect of capillarity in this region. Conversely, at values of Ca_F of order 1 and larger, the film extent is smaller, films do not contribute substantially, and the drying rates are smaller. There we have roughly,

$$F \sim \frac{Dr_t^2 C_e}{\ell} \tag{36}$$

All previous pore-network models (Prat, 1995; Laurindo and Prat, 1996, 1998; Prat and Bouleux, 1999; Yiotis *et al.*, 2001) correspond effectively to such condition.

Figure 14 shows a drying curve calculated using a pore-network model that does not account for liquid films and a drying curve calculated with our model for $Ca_F = 0.1$ under comparable conditions. The presence of liquid films increases the drying rate by approximately a factor of 10 even for a relatively large value of Ca_F.

4. Conclusions

In this work, we first presented results from a 2D pore-network model for isothermal drying in porous media that includes mechanisms like mass transfer by advection and diffusion in the gas phase, viscous flow in liquid and gas phases and capillary effects at the gas–liquid menisci in the pore throats. In a further step, we proceeded to study the effect of capillarity-driven flow in macroscopic liquid films during the drying process. A mathematical model that accounts for viscous flow both through the liquid films and the bulk liquid phase was developed. Using a novel transformation, it was found that film flow is a major transport mechanism, its effect being dominant when capillarity controls the process, which is the case in typical applications.

We have shown that capillarity-induced flow through the films that form in cavities at the pore walls is favored by larger interfacial tension, larger values of the film thickness at the percolation front (where the films emanate) and smaller liquid viscosity. In typical drying problem the extent of the liquid films is approximately proportional to the surface tension. The liquid is transferred from the liquid clusters through the films towards the film tips where it evaporates. The longer is the film region the closer to the open boundary the liquid is transferred and the higher is the drying rate. Our results are in qualitative agreement with previous experimental work which shows accelerated drying when films contribute to flow.

The approach we followed was subject to several simplifying assumptions that may preclude the precise quantitative comparison with experimental results. However, we believe that we have provided a good first approximation to the complicated problem of film flow in drying processes.

References

Blunt, M. J., Jackson, M. D., Piri, M. and Valvante, P. H.: 2002, Detailed physics, predictive capabilities and macroscopic consequences for pore-network models of multiphase flow, *Adv. Water Resour.* **25**, 1069–1089.

Constantinides, G. N. and Payatakes, A. C.: 2000, Effects of precursor wetting films in immiscible displacement through porous media, *Trans. Porous. Med.* **38**, 291–317.

Dillard, L. A. and Blunt, M. J.: 2000, Development of a pore network simulation model to study nonaqueous phase liquid dissolution, *Water Resour. Res.* **36**, 439–454.

Dong, M. and Chatzis, I.: 1995, The imbibition and flow of a wetting liquid along the corners of a square capillary tube, *J. Colloid Interf. Sci.* **172**, 278–288.

Dullien, A. L., Zarcone, C., MacDonald, I. F., Collins, A. and Bochard, D. E.: 1989, The effects of surface roughness on the capillary pressure curves and the heights of capillary rise in glass bead packs, *J. Colloid Interf. Sci.* **127**, 362–772.

Ho, C. K. and Udell, K. S.: 1995, Mass transfer limited drying of porous media containing an immobile binary liquid mixture, *Int. J. Heat Mass Transfer* **38**, 339–350.

Jia, C., Shing, K. and Yortsos, Y. C.: 1999, Visualization and simulation of non-aqueous phase liquids solubilization in pore networks, *J. Contam. Hydrol.* **35**, 363–387.

Laurindo, J. B. and Prat, M.: 1996, Numerical and experimental network study of evaporation in capillary porous media. Phase distributions, *Chem. Eng. Sci.* **51**, 5171–5185.

Laurindo, J. B. and Prat, M.: 1998, Numerical and experimental network study of evaporation in capillary porous media. Drying rates, *Chem. Eng. Sci.* **53**, 2257–2269.

Le Gallo, Y., Le Romancer, J. F., Bourbiaux, B. and Fernades, G.: 1997, Mass transfer in fractured oil reservoirs during gas injection, SPE J 38924.

Lenormand, R.: 1992, Liquids in porous media, *J. Phys.* **2**, SA79–SA88.

Lenormand, R. and Zarcone, C.: 1984, Role of roughness and edges during imbibition in square capillaries, SPE J 13264.

Lenormand, R. and Zarcone, C.: 1985, Invasion percolation in an etched network: measurement of a fractal dimension, *Phys. Rev. Lett.* **54**, 2226–2229.

Li, X. and Yortsos, Y. C.: 1995a, Visualization and simulation of bubble growth in pore networks, *AIChE J*. **41**, 214–222.

Li, X. and Yortsos, Y. C.: 1995b, Theory of multiple bubble growth in porous media by solute diffusion, *Chem. Eng. Sci.* **50**, 1247–1271.

Luikov, A. V.: 1966, Heat and Mass Transfer in Capillary-Porous Bodies. Pergamon Press.

Nowicki, S. C., Davis, H. T. and Scriven, L. E.: 1992, Microscopic determination of transport parameters in drying porous media, *Drying Tech*. **10**, 925–946.

Peitgen, H.-M. and Saupe, D. (eds.): 1988, *The Science of Fractal Images*, Springer-Verlag.

Prat, M.: 1995, Isothermal drying of non-hygroscopic capillary-porous materials as an invasion percolation process, *Int. J. Multiphase Flow* **21**, 875–892.

Prat, M. and Bouleux, F.: 1999, Drying of capillary porous media with a stabilized front in two dimensions, *Phys. Rev. E* **60**, 5647–5656.

Ransohoff, T. C. and Radke, C. J.: 1988, Laminar flow of a wetting liquid along the corners of a predominantly gas-occupied noncircular pore, *J. Colloid Interf. Sci.* **121**, 392–401.

Shaw, T. M.: 1987, Drying as an immiscible displacement process with fluid counterflow, *Phys. Rev. Lett.* **59**, 1671–1674.

Stubos, A. K. and Poulou, S.: 1999, Oil recovery potential from fractured reservoirs by mass transfer processes, SPE J 56415.

Tsimpanogiannis, I. N., Yortsos, Y. C., Poulou, S., Kanellopoulos, N. and Stubos, A. K.: 1999, Scaling theory of drying porous media, *Phys. Rev. E* **59**, 4353–4365.

Valavanides, M. S. and Payatakes, A. C.: 2001, True-to-mechanism model of steady-state two-phase flow in porous media, using decomposition into prototype flows, *Adv. Water Resour.* **24**, 385–407.

van Dijke, M. I. J., Sorbie, K. S. and McDougall, S. R.: 2001, Saturation-dependencies of three-phase relative permeabilities in mixed-wet and fractionally wet systems, *Adv. Water Resour.* **24**, 365–384.

Wilkinson, D. and Willemsen, J. F.: 1983, Invasion percolation: a new form of percolation theory, *J. Phys. A* **16**, 3365–3370.

Witten, T. A. and Sander, L. M.: 1981, Diffusion-limited aggregation. A kinetic critical phenomenon, *Phys. Rev. Lett.* **47**, 1400–1403.

Yiotis, A. G., Stubos, A. K., Boudouvis, A. G., Tsimpanogiannis, I. N. and Yortsos, Y. C.: 2003, Effect of liquid films on the isothermal drying of porous media, *Phys. Rev. E*, **68**, 037303.

Yiotis, A. G., Stubos, A. K., Boudouvis, A. G. and Yortsos, Y. C.: 2001, A 2-D pore-network model of the drying of single-component liquids in porous media, *Adv. Water Resour.* **24**, 439–460.

Yortsos, Y. C. and Stubos, A. K.: 2001, Phase change in porous media, *Curr. Opin. Colloid Interf. Sci.* **6**, 208–216.

Zhou, D., Blunt, M. and Orr Jr., F. M.: 1997, Hydrocarbon drainage along corners of non-circular capillaries, *J. Colloid Interf. Sci.* **187**, 11–21.